ROYAL SOCIETY
OF CHEMISTRY

PAPER

Check for updates

In situ synthesis and *in operando* NMR studies of a high-performance Ni₅P₄-nanosheet anode†

Xuyong Feng, [ID] ‡[a] Mingxue Tang, [ID] ‡[ab] Sean O'Neill[a] and Yan-Yan Hu [ID] ★[ab]

Nickel phosphide (Ni_5P_4) nanosheets are synthesized using *in situ* chemical vapor deposition of P on Ni foam. The thickness of the as-synthesized Ni_5P_4 film is determined to be ~5 nm, using atomic force microscopy (AFM). The small thickness shortens the diffusion path of Li ions and results in fast ion transport. In addition, the 2D Ni_5P_4 nanosheets seamlessly connect to the Ni foam, which facilitates electron transfer between Ni_5P_4 and the Ni current collector. Therefore, the binder/carbon free-nickel supported Ni_5P_4 shows fast rate performance as an anode for lithium-ion batteries (LIBs). The specific capacity of 2D Ni_5P_4 is obtained as 600 mA h g^{-1} at a cycling rate of 0.1C, approaching the theoretical capacity of 768 mA h g^{-1}. Even at a rate of 0.5C, the capacity remains as 450 mA h g^{-1} over 100 cycles. A capacity >100 mA h g^{-1} is retained at a very high rate of 20C. Ni_5P_4 also exhibits a low voltage of ~0.5 V with respect to Li metal, which makes it a suitable negative electrode for LIBs. *In operando* ^{31}P NMR and ^{7}Li NMR are employed to probe the lithiation and de-lithiation mechanisms upon electrochemical cycling.

Introduction

Rechargeable Li-ion batteries (LIBs) have been widely utilized in various portable devices and brought tremendous convenience to our daily life.[1] Searching for safe electrode materials with high energy and power densities is the focus of both fundamental and applied research in recent years.[2] Electric vehicles require LIBs with high energy density and fast charging capability. Although Li metal anodes show high capacity and low voltage, they have limited commercial use due to dendrite formation, leading to the short circuit of batteries.[3] Graphite has been widely employed as the anode in most commercial LIBS but is limited by its low capacity (372 mA h g^{-1} or 840 mA h cm^{-3}). Additionally, Li dendrites are found to form on the surface of graphite during battery operation.[3,4] To overcome these challenges, new and safe anode materials with high energy and power densities have been pursued in the past decade. Among these anode candidates, phosphorus (P) and phosphides with high capacity (2594 mA h g^{-1} based on P) are considered as promising anode candidates.[1,5–15] The potential of P-based anodes (~0.8 V) lies between that of $Li_4Ti_5O_{12}$ (1.55 V) and of graphite (0.1 V). 0.8 V is a desirable potential for anodes

in order to avoid the formation of dendritic lithium and meanwhile offer a higher voltage (compared to the $Li_4Ti_5O_{12}$ anode) when assembled in full batteries.

The high capacity of phosphorus and phosphides originates from multi-electron reactions upon lithiation to form Li_3P or a Li–M–P ternary compound. Among phosphorus anodes, red P suffers from poor chemical stability and extremely low electronic conductivity (1×10^{-14} S cm^{-1}). Black P is limited by its low electronic conductivity and high cost. To achieve fast rate performance, the anode materials are ideally ion and electron mixed conductors. To enhance the electronic conductivity of phosphorous, significant progress has been made by combining P with different conductive carbon (C)-based materials or synthesizing phosphides. High-energy mechanical milling is one of the common techniques for preparing high performance P/C or phosphide anode materials. Park and co-workers transformed amorphous red P into orthorhombic black P at ambient temperature and pressure. The obtained black P delivered a reversible capacity of 1814 mA h g^{-1} with a coulombic efficiency of ~90% in the working voltage range of 0–2 V.[7] The P/C composite obtained with a high energy ball milling method shows a small particle size with fast rate performance.[7,16] In addition to carbon, metals such as Sn, Ti, Mo, and Cu are used with high energy mechanical milling in order to improve the electrochemical performance. Alternatively, P/C composites and phosphides can be obtained *via* thermal reaction processes. Red phosphorus sublimates at around 450 °C, and adsorbs onto the surface of porous carbon to improve the contact between P and C. This facilitates electron transfer and therefore improves the electrochemical performance.[17–19]

aDepartment of Chemistry and Biochemistry, Florida State University, Tallahassee, FL 32306, USA. E-mail: hu@chem.fsu.edu

bNational High Magnetic Field Laboratory, 1800 East Paul Dirac Drive, Tallahassee, FL 32310, USA

‡ These two authors contributed equally and their names are listed in alphabetical order.

In this contribution, we employ a new protocol to synthesize Ni_5P_4 using chemical vapor deposition (CVD) of P onto the surface of Ni foam. The *in situ* synthesized Ni-foam supported Ni_5P_4 shows a 2D nanosheet morphology with large interfacial area, allowing Li ions to quickly diffuse. In addition, the close contact between Ni_5P_4 and Ni foam minimizes the resistance for electron transfer. The mixed fast Li-ion and electron transfer of Ni-supported Ni_5P_4 nanosheet accounts for the observed fast rate performance when Ni/Ni_5P_4 is used as an anode in LIBs. *In operando* ^7Li NMR and ^{31}P solid-state NMR are employed to follow the structural and compositional evolution of Ni_5P_4 during electrochemical cycling. The results provide new insights into the lithiation and de-lithiation mechanisms of Ni_5P_4 anodes.

Experimental section

Material synthesis

Nickel phosphide was prepared by using *in situ* chemical growth of P on the Ni foam surface. Nickel foam was first cut into small pieces (1 cm × 1 cm) and immersed in 5 M HCl solution for 5 min to eliminate surface oxides. The Ni pieces were then washed with deionized water several times to remove residual HCl. Acetone was used to further wash the treated Ni foam, which was dried under vacuum afterwards. For *in situ* growth of nickel phosphide, about 0.2 g red phosphorus was placed 5 cm away from the Ni foam in an alumina crucible. The Al crucible was then placed in a tube furnace and purged with Ar gas for 30 min to remove air before heating. The furnace was heated to 500 °C at a heating rate of 5 °C min^{-1}, and then kept at 500 °C for an additional 10 minutes to ensure that the reaction is complete. The furnace was then naturally cooled down to room temperature. During the entire process, Ar gas was fed at a constant rate of ~1 cm^3 min^{-1} and the red phosphorus was placed upstream relative to the Ni foam. The obtained foam was washed with deionized water and acetone, and then dried under vacuum.

Material characterization

The structure, chemical phase, and morphology of the as-synthesized nickel phosphide were examined by using powder X-ray diffraction (XRD), scanning electron microscopy (SEM), atomic force microscopy (AFM), X-ray photoelectron spectroscopy (XPS), and solid-state nuclear magnetic resonance (NMR). The Ni-supported Ni_5P_4 was peeled from Ni foam and sonicated in ethanol before XRD, AFM, and NMR measurements.

Powder XRD

Powder XRD patterns were recorded on a X'PERT Pro MPD diffractometer (PANalytical) at 45 kV and 40 mA (Cu Kα radiation, $\lambda = 0.15406$ nm). Data were collected in the 2θ range from 10° to 70°, with a scan rate of 6° min^{-1}.

SEM

SEM images of the as-synthesized Ni_5P_4 were acquired on a NOVA NanoSEM 400 field-emission scanning electron microscope with different magnifications.

AFM

The AFM experiments were performed on an MFP-3D AFM equipped with an ARC2 controller. To prepare for the AFM characterization, Ni_5P_4 was dispersed in ethanol and sonicated for 30 min, and then the Ni_5P_4 suspension was coated on a flat glass and dried at room temperature. The data were analysed using NanoScope Analysis 1.5.

XPS

The XPS measurements were performed using a PHI 5000 series spectrometer. XPS spectra were collected at room temperature using a non-monochromatic (Al Kα at 1486.6 eV) X-ray source operated at 400 W, and the chamber pressure was kept below 10^{-8} torr during the measurements. The energy of the spectra was calibrated using the binding energy of the adventitious carbon at 285.0 eV. Data analysis was performed using the CasaXPS software package (version 2.3.18PR1.0). Charge correction was carried out relative to the signal of adventitious carbon (284.8 eV) and a Shirley background model was used. The XPS spectra were fitted using a Gaussian/Lorentzian function (70/30).

In operando solid-state NMR

To prepare for *in operando* NMR characterization, the as-synthesized material was first ground and the unreacted nickel metal was removed with a magnet. The purified nickel phosphide was mixed with polyvinylidene fluoride (PVDF, Kynar Flex 2801 from Arkema) and conductive acetylene black (70 : 10 : 20 in w/w/w). The mixture was dispersed in *N*-methyl-2-pyrrolidone (NMP) and manually ground in an agate mortar for 30 minutes to form a homogeneous slurry. The slurry was cast onto a Ti mesh and dried at 120 °C for 4 hours under vacuum, which was subsequently used as electrodes. The plastic bag cells were assembled using Li and Ni_5P_4 as electrodes and 1 M LiPF$_6$ in EC/DMC/DEC (w/w/w = 1 : 1 : 1) as the electrolyte in an argon-filled glove-box.

The bag cells were electrochemically cycled inside a home-built static NMR probe. ^{31}P NMR spectra were collected while the batteries were cycled at a rate of C/20, assuming the theoretical capacity $C = 768$ mA h g^{-1}. All *in operando* ^{31}P NMR acquisitions were carried out on a Bruker Avance I spectrometer in a 9.4 T magnetic field with a ^{31}P Larmor frequency of 161.4 MHz. The ^{31}P spectra were obtained using a spin echo sequence with a 90° pulse length of 2.5 μs. 6144 transitions were acquired for each spectrum with a recycle delay of 0.5 s. To accommodate the broad spectral width spanning ~3000 ppm, the ^{31}P on-resonance was set on the Ni_5P_4 peak centred at 1400 ppm and the Li_3P peak next to 0 ppm alternately every hour during battery operation. *In operando* ^7Li NMR spectra were recorded by employing a similar procedure. The acquired NMR spectra were fitted and analyzed by using Dmfit software.[20]

Electrochemical tests

The obtained nickel phosphide (Ni_5P_4) supported on the nickel foam was directly used as a working electrode. Lithium metal

This journal is © The Royal Society of Chemistry 2018

J. Mater. Chem. A, 2018, **6**, 22240–22247 | **22241**

was used as the counter electrode. The two electrodes were separated with a microporous membrane (Celgard, 2320), and soaked with the electrolyte of 1 M LiPF$_6$ in EC/DMC/DEC (w/w = 1 : 1 : 1). Coin-type battery cells were assembled in an argon-filled glove-box (MBraun). The electrochemistry tests were performed on a multi-channel battery test system (LAND) within a voltage range of 0.01 V to 2.0 V. The AC impedance was measured at room temperature on a Reference 600 + Gamry Instrument, within a frequency range from 0.1 Hz to 5×10^6 Hz.

Results and discussion

During the *in situ* synthesis, the red phosphorus positioned at the upstream side in the furnace sublimates upon increasing temperature, spreads to the nickel foam, and reacts with nickel to form nickel phosphide. Uniform nanosheets of phosphides on the surface of nickel foam are obtained. The SEM images of the nanosheets are shown in Fig. 1. The *in situ* formed nickel phosphide attaches tightly to the nickel substrate (Fig. 1a), which allows electrons to transfer smoothly between the nickel phosphide electrode and Ni current collector. This close contact is beneficial to high rate performance. The SEM image in Fig. 1b reveals the formation of uniform and ultrathin nickel phosphide sheets. The thickness of the nanosheets is determined by AFM (Fig. 1c and d). The quantitative analysis of the AFM data shows a very narrow distribution of nanosheet thickness around 5 nm (Fig. 1d). The small thickness promotes fast Li-ion transport due to a short diffusion path. Various nickel phosphides (Ni$_5$P$_4$, NiP$_2$, *etc.*) possibly coexist at different reaction conditions, and molar ratios of P/Ni. In this study, the phase was determined to be Ni$_5$P$_4$ based on both powder X-ray diffraction (Fig. S1†) and ^{31}P NMR (Fig. 4) studies[21] when reactions take place at 500 °C for 10 min. NiP$_2$ formation is expected with longer reaction time. More heterogeneous nanosheets with smaller particles are obtained for the 30 min-treated sample (Fig. S2†).

The lithiation of nickel phosphide (Ni$_5$P$_4$) follows a conversion reaction from Ni$_5$P$_4$ to Li$_3$P and Ni. The calculated theoretical capacity of nickel phosphide is 768 mA h g^{-1}. The electrochemical profile of Ni$_5$P$_4$/Li half cells for the 1st and 2nd discharge and charge cycles is shown in Fig. 2a. A very steep drop in voltage is observed at the beginning of the 1st discharge from 2.0 to 0.3 V (Fig. 2a), which is rare for phosphides.[19,22–24] The lithiation between 2.0 V and 0.3 V is attributed to the reaction between NiO on Ni foam and Li, since Ni could be easily oxidized by oxygen (O). Signal related to O$_{1s}$ is observed from the XPS spectrum as shown in Fig. S3.† To further support this argument, the following control experiments are performed. Only a small capacity (0.1 mA h for the 1st discharge as shown in Fig. S4†) is obtained when NiO is removed by the HCl treatment of the nickel foam. Then the capacity is increased to 0.53 mA h when minor oxidation occurs during the heating process at 500 °C. The contribution of NiO to the specific capacity in the first discharge is estimated to be about 80 mA h g^{-1} (Fig. 2a). The capacity gain between 0.3 V and 0 V is attributed to the conversion reaction from Ni$_5$P$_4$ to Li$_3$P and Ni, and minor formation of a solid-electrolyte-interphase (SEI). These two processes related to NiO and Ni$_5$P$_4$ during the first cycle manifest in the cyclic voltammetry (Fig. S5†), from which two separate cathodic peaks appear during the first discharge process. The peak at 1.5 V is the reduction of NiO by Li, which is irreversible and disappears upon further charge and discharge. Upon the first charge, electrochemical activities occur over a broad voltage window between 0 and 2.0 V. The large overpotential of the 1st cycle is attributed to the resistance for both ion and electron transfer in insulating NiO upon discharge and irreversible structural disorder. Due to the removal of NiO and formation of Ni during the 1st discharge, the resistance for both ion and electron transport is significantly reduced, and thus the overpotential for the 2nd discharge is much smaller. Two processes occur during the 2nd discharge, with one around 0.5 V and the other below 0.3 V. These are related to the step-wise conversion from Ni$_5$P$_4$ to Li$_3$P, which is discussed later in the paper.

The changes in resistance for charge transfer in the Ni$_5$P$_4$ anodes upon electrochemical cycling are investigated using electrochemical impedance spectroscopy (EIS). The EIS spectra of a Ni$_5$P$_4$/Li half cell before cycling (labeled "Pristine"), after 1 cycle, and after 100 cycles are displayed in Fig. 2b, which are analyzed using the equivalent circuit model also shown in Fig. 2b and Table S1.† The solution resistance R_s is around 5 ohms for the cell at these three stages. The charge transfer resistance R_{ct} is 134.7 ohms for the pristine cell, and it decreases to 1.43 ohms after the first cycle with very slight increase to 1.56 ohms after 100 cycles. The nearly 100-fold drop in charge transfer resistance is probably due to the removal of the insulating NiO on the surface of Ni$_5$P$_4$ upon the initial discharge process. As SEIs are expected to form upon electrochemical cycling, an additional component in the equivalent
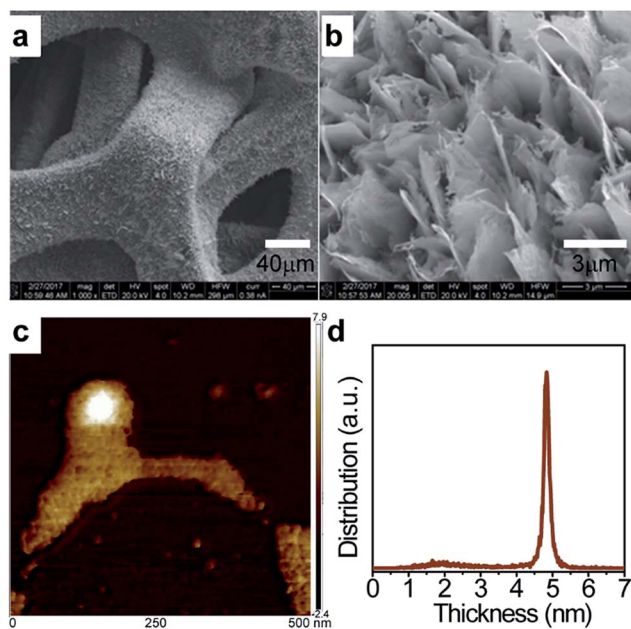

Fig. 1 Microscopy images of the *in situ* synthesized Ni$_5$P$_4$ nanosheets supported on Ni foam: (a) and (b) are SEM images with different magnifications of the nickel phosphide on Ni foam, (c) the AFM image, and (d) the histogram of nanosheet thickness obtained from the analysis of AFM results.
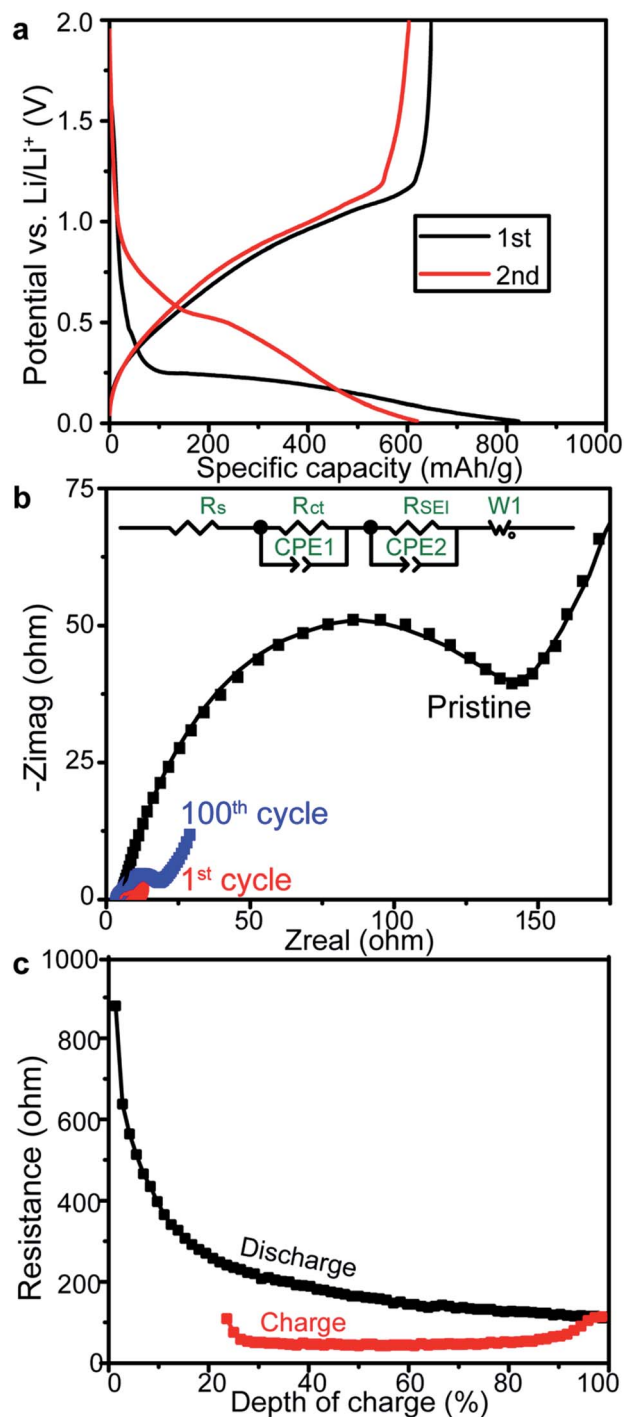
22242 | *J. Mater. Chem. A*, 2018, **6**, 22240–22247

This journal is © The Royal Society of Chemistry 2018

Fig. 2 Electrochemical performance of the Ni$_5$P$_4$ anode in Ni$_5$P$_4$/Li half cells. (a) discharge–charge profile for the first 2 cycles, (b) Electrochemical Impedance Spectroscopy (EIS) spectra of a pristine Ni$_5$P$_4$/Li battery, and the same battery after the 1st and 100th discharge–charge cycles, and (c) DC resistance at different depths of charge during the first discharge–charge cycle, obtained from GITT measurements (Fig. S6†).

circuit model is added to account for their effects on charge transfer in the Ni$_5$P$_4$/Li cell after 1 cycle and 100 cycles. The calculated resistance values for charge transfer within the SEIs are 4.35 ohms and 12.55 ohms for the cell after 1 cycle and 100 cycles, respectively.

DC resistance is also measured using the galvanostatic intermittent titration technique (GITT), offering additional insights into the over-potential (Fig. 2c). The electronic resistance for the pristine Ni$_5$P$_4$/Li cell is 900 ohms, which gradually reduces to around 100 ohms during the first discharge. Then the electronic resistance continues to decrease at the beginning of the 1st charge and remains around 50 ohms upon further charge. Towards the end of charge, the resistance increases slightly to 100 ohms. The first drop in electronic resistance from
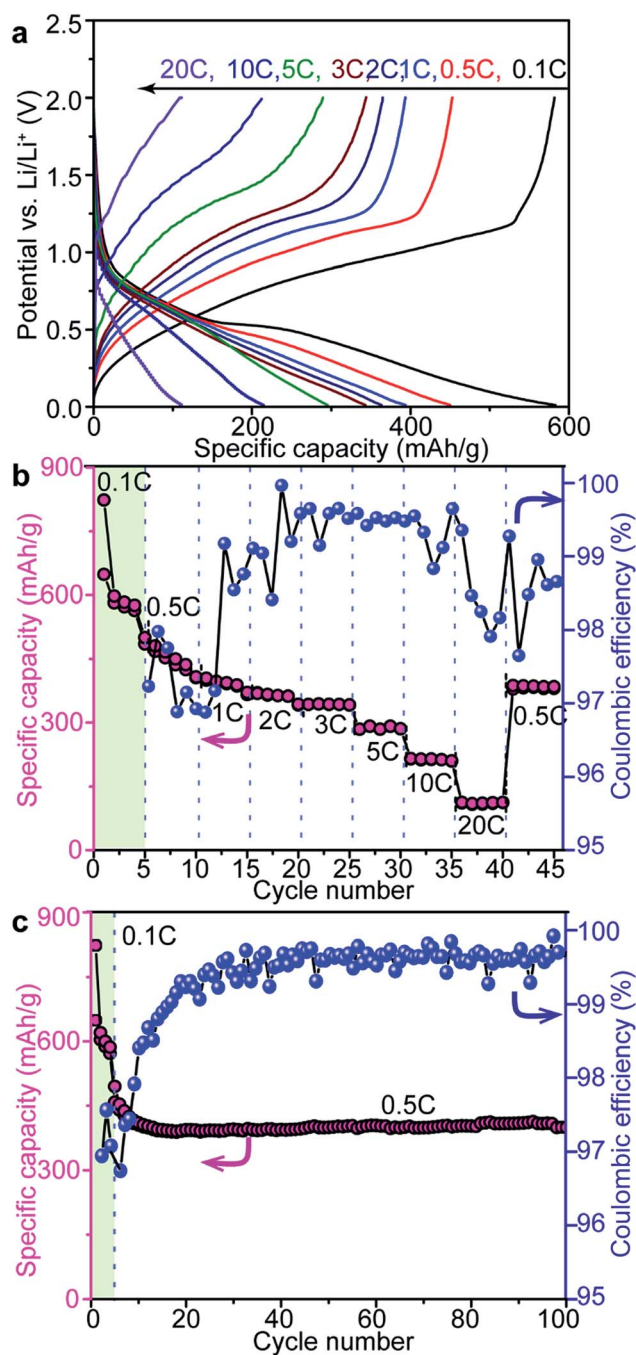

Fig. 3 The rate performance of the Ni$_5$P$_4$: (a) discharge–charge profiles at different cycling rates. (b) The specific capacity as a function of the charge rate and (c) the high-rate performance over extended cycling.

This journal is © The Royal Society of Chemistry 2018

J. Mater. Chem. A, 2018, 6, 22240–22247 | 22243

900 to 100 ohms is due to the removal of insulating NiO and the formation of conductive Ni. The small reduction from 100 to 50 ohms at the beginning of the first charge is attributed to the decomposition of a resistive SEI. The resistance increase at the end of charge from 50 to 100 ohms is due to the formation of a SEI at high voltage. Both ^{31}P NMR and ^{7}Li NMR suggest SEI formation, which is discussed later.

The rate performance of Ni_5P_4 as the anode is studied. A reversible capacity ~600 mA h g^{-1} can be achieved at a rate of 0.1C. A fast cycling rate produces smaller capacity. As shown in Fig. 3, the capacity decreases from 600 to 451 mA h g^{-1} when the rate increases from 0.1C to 0.5C. Keeping the rate of discharge to be 0.5C and increasing the charge rate gradually to 20C, the capacity decreases to 112 mA h g^{-1}. When the charge rate is set to 0.5C again, a capacity of 400 mA h g^{-1} is obtained (Fig. 3c), indicating the long-term reversible performance of Ni_5P_4. The coulombic efficiency of the first cycle is around 80%, which is higher than those of typical oxide anodes.[25] Almost 100% coulombic efficiency is obtained for the subsequent 100 cycles.

In order to probe the lithiation and de-lithiation mechanism of Ni_5P_4, *in operando* characterization is performed. For most phosphide anodes, their structures undergo disordering upon the discharge–charge cycling process, which makes it difficult to determine with regular microscopy or diffraction tools. Solid-state NMR has been proven to be a powerful tool to determine the short-range structures of disordered materials.[26–29] In this contribution, *in operando* ^{31}P NMR and ^{7}Li NMR spectroscopy are employed to follow the evolution of (de)lithiation of Ni_xP during charge–discharge processes. The structure of Ni_5P_4 is shown in Fig. 4a, in which P is coordinated to various numbers of Ni. P coordinated with 1, 5, 7, and 9 Ni atoms are denoted as P1, P5, P7, and P9. The ^{31}P NMR spectrum of the pristine anode Ni_5P_4 spans over 1500 ppm (500 to 2000 ppm) with the most intense signal at ~1700 ppm (Fig. 4b). The ^{31}P shift away from 0 ppm is called the Knight shift, a result of the interactions between P spins and conductive electrons. A large Knight shift is observed for Ni_5P_4 compared with that of Cu_3P [~400 ppm], which is mainly due to the decrease of d-band contribution to the density of states (DOS) at the Fermi level.[30] The ^{31}P shift is
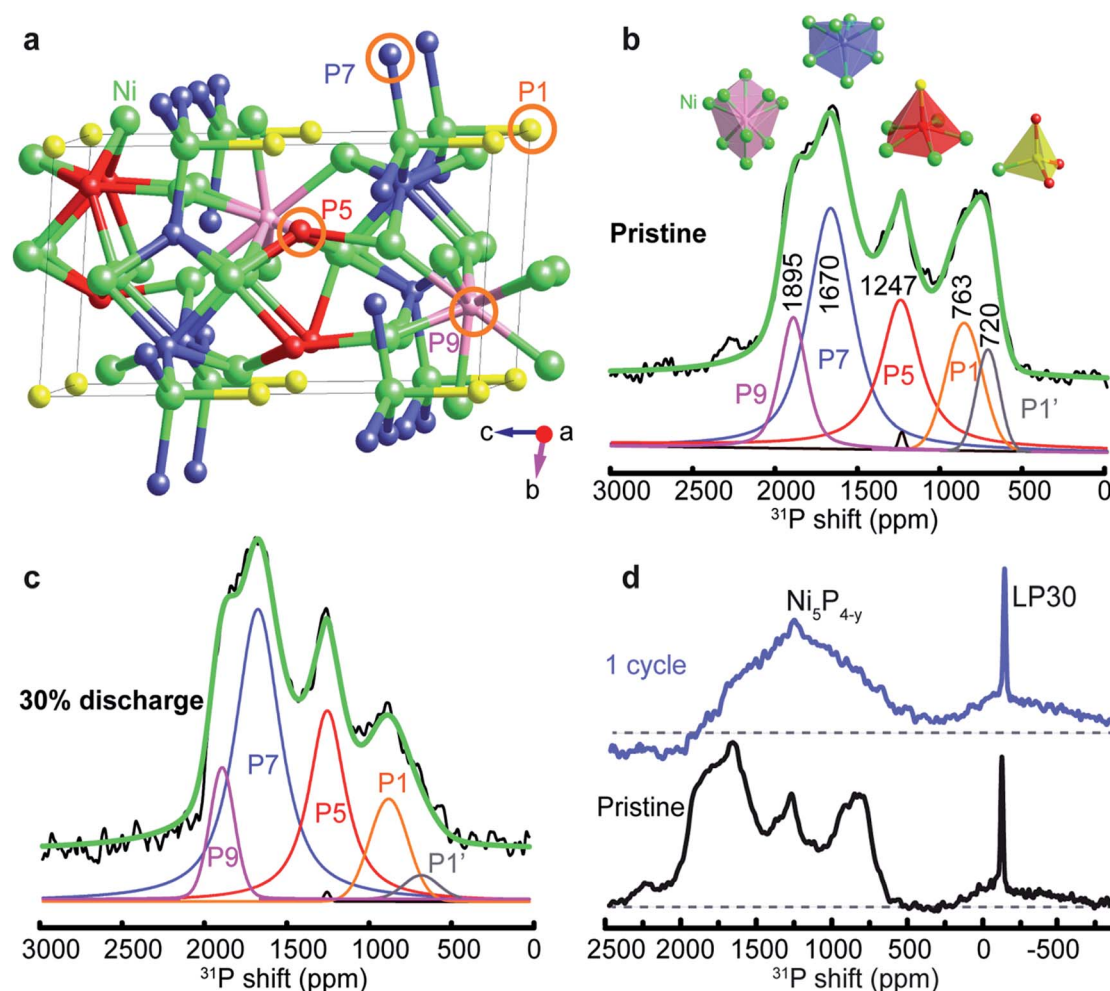

Fig. 4 The structure of Ni_5P_4 and the representative *in operando* ^{31}P solid-state NMR spectra. (a) The structure of Ni_5P_4; P1, P5, P7, and P9 are phosphorus sites coordinated with 1, 5, 7, and 9 Ni atoms (green), respectively. (b) and (c) the ^{31}P spectra and the corresponding spectral simulation of the pristine Ni_5P_4 anode and the anode at 50% discharge, respectively. (d) The spectral comparison of a Ni_5P_4//Li battery at the pristine state and at the end of the 1st discharge–charge cycle.

22244 | *J. Mater. Chem. A*, 2018, **6**, 22240–22247

This journal is © The Royal Society of Chemistry 2018

highly dependent on the number of Ni locating in the vicinity of P atoms.[21,30] Five ^{31}P resonances are observed based on spectral analysis shown in Fig. 4b: the peak at 1895 ppm is assigned to P9 surrounded by 9 Ni atoms, 1670 ppm for P7 surrounded by 7 Ni atoms, 1247 ppm for P5 close to 5 Ni atoms, and the last two peaks at 763 ppm and 720 ppm are assigned to P1 (P next to 1 Ni) and P1′ (distorted configuration). It's worth mentioning that the shift is not linearly proportional to the number of nearby Ni atoms because of different bond lengths and angles, which affect spin density transfer (Fig. 4a and top of Fig. 4b). In the middle of the 1st discharge, the four resonances are still visible. P1 shows the largest reduction compared to P5, P7, and P9 (Fig. 4c). At the end of the 1st cycle, the resonances become significantly overlapped compared with those for the pristine anode (Fig. 4d) due to increased structural disorder.

To follow the structural evolution in real time, *in operando* [31]P spectra are acquired and shown with the corresponding electrochemical profile in Fig. 5a. In the ^{31}P NMR spectrum of the pristine battery, one additional sharp peak at −140 ppm is observed from electrolyte $LiPF_6$ as shown in the bottom of Fig. 5a. Upon discharge, Li is stripped from the Li anode and inserted into Ni_5P_4 to form Ni_5P_{4-y} and Li_3P; the ^{31}P resonance for Li_3P mainly appears at around −200 ppm. Most P in Ni_5P_4 converts to Li_3P upon further discharge, and the ^{31}P signal of Ni_5P_4 disappears completely at the end of discharge. The [31]P

signal of Li_3P simultaneously grows upon discharge. A recycle delay of 0.5 s is used for the NMR acquisition to optimize temporal resolution, which is sufficient for Ni_5P_{4-y} (T_1 = 0.5 ms) to fully relax, but very short for Li_3P (T_1 = 60 s), and therefore the ^{31}P spectra are not a quantitative representation of Li_3P. Upon charge, P is released from Li_3P and combined with Ni. Meanwhile, Li is extracted from Li_3P and deposited on the Li anode. The original five ^{31}P NMR peaks of Ni_5P_4 become unrecognizable upon charge because the P local structure is perturbed by Li insertion and extraction and becomes increasingly disordered.

Quantitative analysis is performed on the *in operando* ^{31}P NMR spectra. ^{31}P NMR areal integrals of both Ni_5P_{4-y} and Li_xP are shown in Fig. 5b and c. The signal of Ni_5P_{4-y} shows different reaction rates upon discharge as shown in Fig. 5b. The 1st discharge can be divided into three regions (I, II, and III) by the kink points at ~200 mA h g^{−1} and ~390 mA h g^{−1}. At the beginning of discharge (Region I), only P1, P1′, and P5 participate in the reaction. P7 and P9 remain nearly unchanged. P7 and P9 start to take part in the reaction in Region II (190–340 mA h g^{−1}) and a major reduction in their amount is observed. P1 and P1′ are reduced to a very small amount at the end of Region II and stay almost unchanged through Region III (340–750 mA h g^{−1}). The major conversion of P5, P7, and P9 sites continue in Region III. The reaction rates of P7 and P9 are

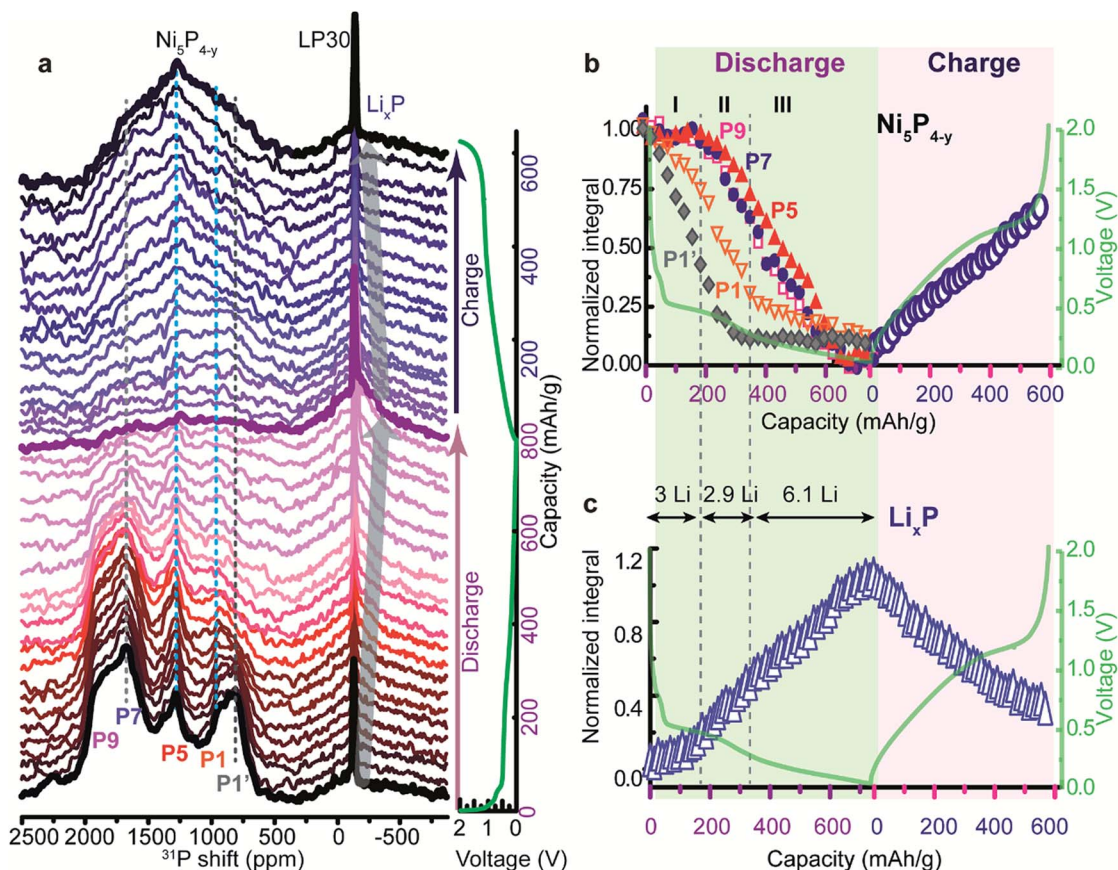**Fig. 5** (a) *In operando* ^{31}P NMR spectra of a Ni_5P_4//Li half-cell battery during the 1st cycle and the corresponding electrochemical profile. (b) and (c) Normalized area integrals of ^{31}P NMR resonances from Ni_5P_{4-y} and Li_xP, respectively.

almost identical throughout the entire discharge process. During the 1st charge, all P sites converge to one broad ^{31}P signal centered around ~1500 ppm and the total integral recovers to ~75% of the original, indicating that ~25% P is not restored back to Ni_5P_{4-y}, which is in good agreement with the electrochemical quantification. Accordingly, the signal of Li_3P grows linearly from zero upon lithiation and about 25% remains at the top of charge (Fig. 5c). The *operando* ^{31}P NMR results reveal that the P sites in Ni_5P_4 with fewer Ni coordination sites convert to Li_3P first at relatively high cell potential compared with reactions to break Ni–P bonds in P5, P7, and P9 configurations. As Gibbs free energy $\Delta G = -nFE$, where n is the number of electrons transferred, F is the Faraday constant, and E is the cell potential. $n = 1$ for one-bond breaking of Ni–P, E_{cell} = E(cathode) − E(Li/Li$^+$) = E(cathode) + 3.4 V. If the cathode reaction occurs at a high potential, it leads to a high cell voltage and thus a large magnitude of Gibbs free energy. This suggests that reactions taking place at a high potential are more spontaneous and require less external energy input than those occurring at a low potential. This finding provides insights into the reaction thermodynamics of Ni_5P_4 anodes under working conditions in real time. This offers a solid explanation at an atomic level for the macroscopic observation made from electrochemical profiles for nickel phosphides: P coordinated with more Ni shows lower average potential *vs.* Li/Li$^+$, *e.g.* the average potential *vs.* Li/Li$^+$ of Ni_5P_4 [31] is found to be 0.5 V, which is lower than 0.6 V for NiP$_2$.[14]

In addition to ^{31}P local structural evolution, *operando* ^{7}Li NMR is performed to follow the dynamics and evolution of (de) lithiation. To achieve this, an identical bag-cell was assembled for the ^{7}Li NMR study. Two components for the pristine battery are clearly resolved as shown in Fig. 6a. Li anode shows a sharp peak at around 270 ppm.[14,27] Another sharp peak locating at 0 ppm is attributed to the electrolyte LP30. Upon discharge, Li is stripped from the Li anode and inserted into Ni_5P_4 to form Li_3P, for which ^{7}Li resonance is at around 0 ppm and the intensity increases upon discharge. Li is electrochemically extracted from Li_3P and then deposits on the Li anode upon charge.

Quantitative analysis of the *in operando* ^{7}Li spectra is performed and the results are shown in Fig. 7. A similar electrochemical profile is obtained compared to the 1st bag-cell battery shown in Fig. 5, indicating good reproducibility. A quick drop of voltage is found at the beginning of the 1st discharge from 2.0 to 0.5 V, and the voltage decreases gradually to zero upon further discharge.

Normalized ^{7}Li NMR integrals for both Li_3P and Li metal are shown in Fig. 7b and c. The signal of Li_3P grows linearly from zero upon discharge. During charge, Li_3P is reversibly converted to Li and Ni_5P_{4-y}; however about ~25% of the Li_3P signal remains at the end of the 1st charge, indicating that ~25% Li remains in Li_3P. It is worth noting that the rate of decrease in the Li_3P amount at the very end of first charge is slowed down, as evidenced by both ^{31}P and ^{7}Li NMR (Fig. 5 and 7), this is likely due to the formation of SEIs which have overlapped NMR signals around 0 ppm with Li_3P. The Li anode signal remains constant during the 1st discharge, due to skin depth effects.[32] However, it grows linearly from zero upon charge due to loose Li
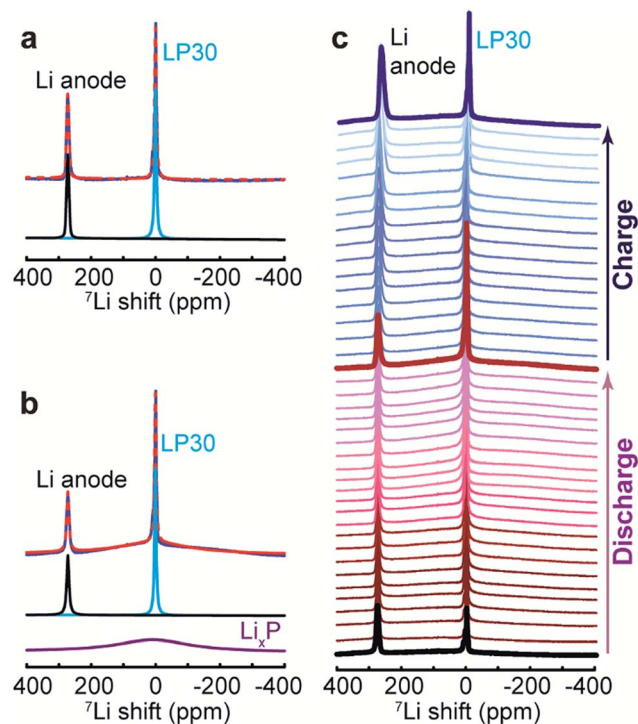

Fig. 6 ^{7}Li NMR spectra and the corresponding spectral simulation for a pristine (a) and a fully discharged (b) Ni_5P_4//Li half-cell battery. The experimental spectra are in blue, and the corresponding simulations are in red (dashed lines). The simulated spectra are composed of three components, *i.e.*, Li metal (black line), Li$^+$ from electrolyte LP30 (grey line), and Li_3P (purple line). (c) Selective *in operando* ^{7}Li NMR spectra during the first discharge−charge cycle.

microstructures formed on the Li anode surface. In summary, both ^{7}Li and ^{31}P NMR results consistently illustrate the key modifications of local structures in nickel phosphide upon lithiation and de-lithiation.
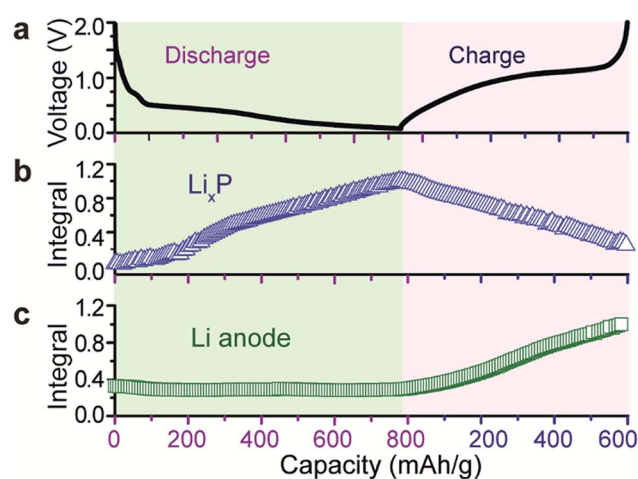

Fig. 7 (a) Electrochemical profile of a Ni_5P_4//Li half-cell battery in the working voltage window between 2.0 and 0.0 V. (b) and (c) Normalized area integrals of the Li_xP and Li resonances from *in operando* ^{7}Li NMR shown in Fig. 6.

22246 | *J. Mater. Chem. A*, 2018, **6**, 22240–22247

This journal is © The Royal Society of Chemistry 2018

Conclusions

Two-dimensional Ni_5P_4 nanosheets are prepared *via in situ* chemical vapor deposition of red P onto the surface of nickel foam. The structure and morphology of Ni_5P_4 are characterized by XRD, SEM and AFM. Compared with commercial graphite anodes, the as-synthesized Ni_5P_4 nanosheets shows higher capacity, better rate performance, and enhanced long-term cycling stability,[33–35] making it as a promising anode material for high power Li-ion batteries. The reaction dynamics and local structural modifications of working Ni_5P_4/Li cells are probed by both ^{7}Li and ^{31}P NMR. *In operando* ^{31}P NMR spectra reveal that the ordered Ni_5P_4 becomes amorphous after the 1st cycle. In addition, different P sites are sequentially lithiated; P sites surrounded by fewer Ni atoms react more easily with Li than those with more Ni neighbors. Complementary ^{7}Li NMR is employed to follow the evolution of Li for both the Li anode and Li_3P formed from Ni_5P_4. *In situ* synthesis in conjunction with *in operando* characterization of nickel phosphide (Ni_5P_4) has led to an anode of fast-rate performance with insights for designing other nickel phosphides.

Conflicts of interest

There are no conflicts to declare.

Acknowledgements

Notes and references

1 M. Armand and J.-M. Tarascon, *Nature*, 2008, **451**, 652–657.
2 J.-M. Tarascon and M. Armand, *Nature*, 2001, **414**, 359–367.
3 W. Xu, J. Wang, F. Ding, X. Chen, E. Nasybulin, Y. Zhang and J.-G. Zhang, *Energy Environ. Sci.*, 2014, **7**, 513–537.
4 X. Wang, Z. Na, D. Yin, C. Wang, G. Huang and L. Wang, *Energy Storage Materials*, 2018, **12**, 103–109.
5 F. Gillot, S. Boyanov, L. Dupont, M.-L. Doublet, M. Morcrette, L. Monconduit and J.-M. Tarascon, *Chem. Mater.*, 2005, **17**, 6327–6337.
6 H. Hwang, M. G. Kim, Y. Kim, S. W. Martin and J. Cho, *J. Mater. Chem.*, 2007, **17**, 3161.
7 C.-M. Park and H.-J. Sohn, *Adv. Mater.*, 2007, **19**, 2465–2468.
8 S. Boyanov, J. Bernardi, E. Bekaert, M. Ménétrier, M.-L. Doublet and L. Monconduit, *Chem. Mater.*, 2009, **21**, 298–308.
9 C.-M. Park, Y.-U. Kim and H.-J. Sohn, *Chem. Mater.*, 2009, **21**, 5566–5568.
10 S. Carenco, D. Portehault, C. Boissière, N. Mézailles and C. Sanchez, *Chem. Rev.*, 2013, **113**, 7981–8065.
11 J. Fullenwarth, A. Darwiche, A. Soares, B. Donnadieu and L. Monconduit, *J. Mater. Chem. A*, 2014, **2**, 2050–2059.
12 M. Mayo, K. J. Griffith, C. J. Pickard and A. J. Morris, *Chem. Mater.*, 2016, **28**, 2011–2021.
13 N. Nitta, D. Lei, H.-R. Jung, D. Gordon, E. Zhao, G. Gresham, J. Cai, I. Luzinov and G. Yushin, *ACS Appl. Mater. Interfaces*, 2016, **8**, 25991–26001.
14 P. Lou, Z. Cui, Z. Jia, J. Sun, Y. Tan and X. Guo, *ACS Nano*, 2017, **11**, 3705–3715.
15 J. Xu, I.-Y. Jeon, J. Ma, Y. Dou, S.-J. Kim, J.-M. Seo, H. Liu, S. Dou, J.-B. Baek and L. Dai, *Nano Res.*, 2017, **10**, 1268–1281.
16 J. Qian, D. Qiao, X. Ai, Y. Cao and H. Yang, *Chem. Commun.*, 2012, **48**, 8931–8933.
17 B. Ruan, J. Wang, D. Shi, Y. Xu, S. Chou, H. Liu and J. Wang, *J. Mater. Chem. A*, 2015, **3**, 19011–19017.
18 Z. Yu, J. Song, M. L. Gordin, R. Yi, D. Tang and D. Wang, *Adv. Sci.*, 2015, **2**, 1400020.
19 W. Li, Z. Yang, M. Li, Y. Jiang, X. Wei, X. Zhong, L. Gu and Y. Yu, *Nano Lett.*, 2016, **16**, 1546–1553.
20 D. Massiot, F. Fayon, M. Capron, I. King, S. Le Calvé, B. Alonso, J.-O. Durand, B. Bujoli, Z. Gan and G. Hoatson, *Magn. Reson. Chem.*, 2002, **40**, 70–76.
21 E. Bekaert, J. Bernardi, S. Boyanov, L. Monconduit, M.-L. Doublet and M. Ménétrier, *J. Phys. Chem. C*, 2008, **112**, 20481–20490.
22 K. Wang, J. Yang, J. Xie, B. Wang and Z. Wen, *Electrochem. Commun.*, 2003, **5**, 480–483.
23 M. G. Kim, S. Lee and J. Cho, *J. Electrochem. Soc.*, 2009, **156**, A89.
24 J. Tian, Q. Liu, N. Cheng, A. M. Asiri and X. Sun, *Angew. Chem., Int. Ed.*, 2014, **53**, 9577–9581.
25 C. Wang, D. Wang, Q. Wang and H. Chen, *J. Power Sources*, 2010, **195**, 7432–7437.
26 C. P. Grey and N. Dupré, *Chem. Rev.*, 2004, **104**, 4493–4512.
27 R. Bhattacharyya, B. Key, H. Chen, A. S. Best, A. F. Hollenkamp and C. P. Grey, *Nat. Mater.*, 2010, **9**, 504–510.
28 J. Zheng, M. Tang and Y.-Y. Hu, *Angew. Chem., Int. Ed.*, 2016, **55**, 12538–12542.
29 X. Li, M. Tang, X. Feng, I. Hung, A. Rose, P.-H. Chien, Z. Gan and Y.-Y. Hu, *Chem. Mater.*, 2017, **29**, 8282–8291.
30 I. Furo, I. Bakonyi, K. Tompa, E. Zsoldos, I. Heinmaa, M. Alla and E. Lippmaa, *J. Phys.: Condens. Matter*, 1990, **2**, 4217.
31 J. Jiang, C. Wang, W. Li and Q. Yang, *J. Mater. Chem. A*, 2015, **3**, 23345–23351.
32 A. J. Ilott, S. Chandrashekar, A. Klöckner, H. J. Chang, N. M. Trease, C. P. Grey, L. Greengard and A. Jerschow, *J. Magn. Reson.*, 2014, **245**, 143–149.
33 X. Liu, D. Wang, B. Zhang, C. Luan, T. Qin, W. Zhang, D. Wang, X. Shi, T. Deng and W. Zheng, *Electrochim. Acta*, 2018, **268**, 234–240.
34 C. E. L. Foss, A. M. Svensson, Ø. Gullbrekken, S. Sunde and F. Vullum-Bruer, *Journal of Energy Storage*, 2018, **17**, 395–402.
35 L. Madec and H. Martinez, *Electrochem. Commun.*, 2018, **90**, 61–64.